

The axis of evil - a polarization perspective

M. Frommert & T. A. Enßlin

Max-Planck-Institut für Astrophysik, Karl-Schwarzschild-Straße 1, D-85748 Garching bei München, Germany
 mona@mpa-garching.mpg.de

Accepted ??? Received ???; in original form ???

ABSTRACT

We search for an unusual alignment of the preferred axes of the quadrupole and octopole, the so-called *axis of evil*, in the CMB temperature and polarization data from WMAP. We split the temperature and polarization maps into a part correlated with the respective other map, and a part uncorrelated with that. We then determine the preferred axes for the quadrupole and octopole in all four of those maps. If the alignment detected previously in the temperature maps were due to a preferred direction intrinsic to our Universe, we would expect it to be present in all four of our maps. In particular, the part of the polarization map which is uncorrelated with the temperature map serves as a truly independent probe of the axis of evil. We find a possible alignment in the two maps dominated by the temperature data, however, with a large uncertainty in the axes due to the high noise-level in the polarization data. In the two polarization data dominated maps, we find that the axis of the quadrupole roughly aligns with the axis of evil within our measurement precision, whereas the axis of the octopole does not. However, with our measurement uncertainty, the probability of such a scenario to happen by chance in an isotropic universe is of the order of 50 per cent. We also find that the so-called cold spot present in the CMB temperature map is even colder in the uncorrelated temperature map, although there is still a large uncertainty in the latter. Therefore, our analysis of the axis of evil, and a future analysis of the cold spot in the uncorrelated temperature data will strongly benefit from the polarization data expected from the *Planck* satellite.

Key words: Cosmology: CMB

1 INTRODUCTION

A major assumption of modern day cosmology is the cosmological principle, which states that the Universe is homogeneous and isotropic on large scales. The observed isotropy of the Cosmic Microwave Background (CMB) is one of the strongest evidences supporting the cosmological principle.

However, in recent years, there have been claims of anomalies detected in the CMB temperature map with considerable significance, which seem to break statistical isotropy of the temperature fluctuations and thus to question the cosmological principle. Several groups (de Oliveira-Costa et al. 2004; Abramo et al. 2006; Land & Magueijo 2007; Samal et al. 2008; Rakić & Schwarz 2007) claim to have found a strong alignment between the preferred axes of the quadrupole and the octopole, which is commonly referred to as the *axis of evil*. Others (Bernui 2008; Eriksen et al. 2007; Hoftuft et al. 2009) have found a significant power asymmetry between the northern and southern ecliptic hemisphere. However, the existence of such an isotropy breaking in the CMB temperature map is strongly under debate, and also negative results have been published (Souradeep et al. 2006; Magueijo & Sorkin 2007). The claims of the existence of a preferred direction in the CMB temper-

ature map have led to a discussion about whether this is simply due to a chance fluctuation in the CMB temperature map, whether it can be blamed on local structures or on systematics in the measurement, or whether it is actually due to a preferred direction intrinsic to our Universe (Dolag et al. 2005; Maturi et al. 2007; Samal et al. 2009; Groeneboom & Eriksen 2009; Morales & Sáez 2008; Vielva et al. 2007; Inoue & Silk 2007).

Since the polarization fluctuations of the CMB have the same physical origin as the primordial temperature fluctuations, they should exhibit similar peculiarities as the latter, if these are intrinsic to our Universe. Only if the peculiarities in the temperature maps are due to a secondary effect on the CMB such as the integrated Sachs-Wolfe effect, we would not expect them to be present in the polarization maps (Dvorkin et al. 2008). Given that the CMB polarization is subject to partly different systematics and foregrounds than the observed temperature map, it can be used as a partly independent check for the above-mentioned anomalies. The search for anomalies in the CMB polarization map is still in its initial stage, due to the high noise-level in the available full-sky polarization map from the *Wilkinson Microwave Anisotropy Probe* (WMAP). Souradeep et al. (2006) have found some evidence for anisotropies in the WMAP polarization data using the method proposed in

map	explanation	eq.	multipole	(l, b)	σ
P_{corr}	"T \rightarrow P"	(21)	quadr	$(-117^\circ, 60^\circ)$	-
			oct	$(-124^\circ, 66^\circ)$	-
$P_{\text{uncorr}}^{\text{rec}}$	"P - P_{corr} "	(24)	quadr	$(-79^\circ, 36^\circ)$	42°
			oct	$(-17^\circ, 0^\circ)$	48°
$T_{\text{corr}}^{\text{rec}}$	"P \rightarrow T"	(17)	quadr	$(-73^\circ, 42^\circ)$	42°
			oct	$(-17^\circ, -19^\circ)$	37°
$T_{\text{uncorr}}^{\text{rec}}$	"T - $T_{\text{corr}}^{\text{rec}}$ "	(20)	quadr	$(-107^\circ, 42^\circ)$	33°
			oct	$(-112^\circ, 54^\circ)$	10°

Table 1. Axes and their uncertainties for the four different maps in galactic coordinates. The large errors are due to the effects of the mask, residual foregrounds and the detector noise in the WMAP polarization data.

Basak et al. (2006). However, they state that the anisotropies are likely due to observational artifacts such as foreground residuals, and that further work is required in order to confirm a possible cosmological origin.

Given that the polarization map is correlated with the temperature map, it can only be used as a partly independent probe of the anomalies which have been found in the temperature map. If the observed anomalies were due to a chance fluctuation in the temperature map, this chance fluctuation would also be present in the polarization maps, due to the correlation between the two (Dvorkin et al. 2008). In this work, we split the WMAP polarization map into a part correlated with the temperature map, P_{corr} , and a part uncorrelated with the latter, $P_{\text{uncorr}}^{\text{rec}}$. We obtain the part of the polarization map which is correlated with the temperature map by simply translating the temperature map into a polarization map, using the cross-correlation between the two. The part of the polarization map which is uncorrelated with the temperature map serves as a truly independent probe of the above-mentioned anomalies. Chance fluctuations in the temperature maps do not affect the uncorrelated polarization map, so that a detection of the anomalies in the latter would be a hint to an actual cosmological origin of them.

Similarly, we split the WMAP temperature map into a part correlated with the polarization map, $T_{\text{corr}}^{\text{rec}}$, and an uncorrelated map, $T_{\text{uncorr}}^{\text{rec}}$. If the anomalies detected in the CMB temperature map are of genuine cosmological origin, they should be present in the correlated and the uncorrelated parts of both the temperature and polarization map. For convenience, the four resulting maps are summarised and briefly described in table 1.

In this work, we focus on using the uncorrelated polarization map to probe the axis of evil. In order to define the preferred axis of the multipoles, we use a statistic proposed by de Oliveira-Costa et al. (2004), which is the axis around which the angular momentum dispersion is maximised for a given multipole l . We note that we have to mask out about 25 per cent of the sky in the WMAP polarization data in order to reduce galactic foregrounds. Furthermore, the polarization data are highly contaminated by detector noise and residual foregrounds even outside the mask. We therefore perform a Wiener filtering of the polarization data before determining the preferred axes, in order to reduce the noise contained in the maps. However, we still expect a large uncertainty in the axes, which we obtain by running Monte Carlo (MC) simulations conditional on the data. The uncertainty in our axes amounts to $\sigma \approx 45^\circ$. The main contribution of the uncertainty in the axes comes from the high noise-level in the polarization data rather than from the mask. We can therefore hope that the *Planck* polarization data (Tauber 2000) will yield much stronger constraints on the axes than the WMAP data.

We find that, for all four of the maps, the preferred axes of

the quadrupole all point in the same direction, within our measurement precision. However, the preferred axis of the octopole of the uncorrelated polarization map does not align with the one of the quadrupole. The same holds for the correlated temperature map.

In order to assess our result, we ask the following question. We take the axes measured in the temperature map as given, and assume that the axes of the uncorrelated polarization map are distributed isotropically and independently of each other. We then ask how likely it is that at least one of these axes lies such that the axis of the temperature map lies inside its 1σ region. This probability amounts to about 50 per cent for currently available polarization data. This high probability is due to the large uncertainties we have in the axes of the uncorrelated polarization map.

We would like to point out that the above-described claims of anomalies detected in the temperature maps might only be of such high significance because the statistics, which have been used to assess the peculiarities, have been chosen a posteriori. There are an infinite number of so-called statistics, i.e. transformations of the data, which can be calculated and then checked for compatibility with the null hypothesis (in our case isotropy of the Universe). In light of this, the above-described findings of an incompatibility of one particular statistic with the null hypothesis in the temperature map seem alleviated.

The article is organised as follows. In section 2, we briefly review the Wiener filter. In sections 3 and 4, we explain in detail the splitting of the WMAP temperature and polarization maps, respectively. Section 5 is devoted to determining the preferred axes for the quadrupole and octopole for our four maps. We conclude in section 6.

2 WIENER FILTERING

As we have already mentioned in the introduction, the WMAP polarization data are highly contaminated by detector noise and galactic foregrounds. The observed polarization map we use is the linear combination of the maps of the Ka, Q, and V frequency bands (corresponding to 33, 41, and 61 GHz), which are used for determining the low- l polarization likelihood in the 5 year WMAP likelihood code (Hinshaw et al. 2009). By using the linear combination of the maps, we combine the information from different frequency bands rather than using only the information contained in a particular band. Therefore, the linear combination is less contaminated by noise than the original maps per frequency band. We use the P06 mask (Page et al. 2007) to mask out the galactic plane in the polarization map. The linear combination maps for the Stokes Q and U parameters are shown in Fig. 1 in galactic coordinates.

In order to reduce the noise level, we perform a Wiener filtering of the observed polarization map before translating it into the part of the temperature map which is correlated with the polarization data. Similarly, we will perform a Wiener filtering of the part of the polarization map which is uncorrelated with the temperature map, as we will describe in detail later on.

The Wiener filter can be derived for the general data model

$$d = Rs + n, \quad (1)$$

where d denotes the data, s the (temperature or polarization) signal, R the instrument response and n additive noise. Let us define the signal and noise covariances,

$$S \equiv \langle ss^\dagger \rangle_{\mathcal{P}(s)} \equiv \int \mathcal{D}s (ss^\dagger) \mathcal{P}(s), \quad (2)$$

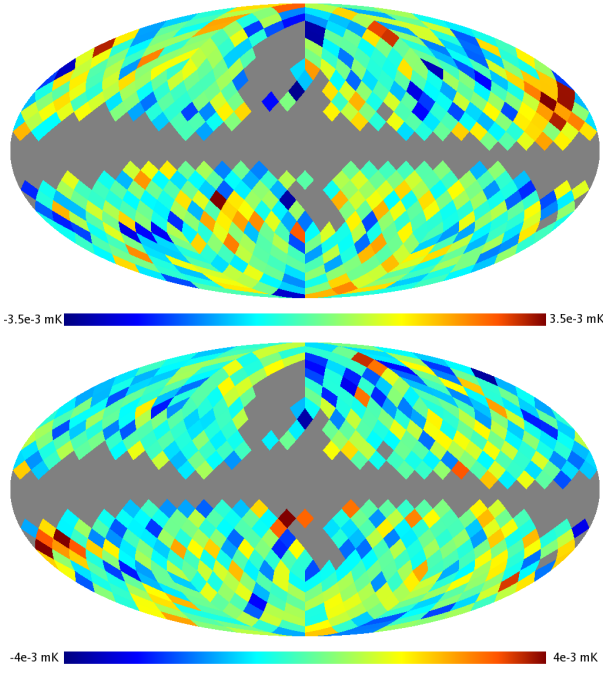


Figure 1. Observed polarization maps (linear combination of Ka, Q, and V band maps). Stokes Q map (top panel) and Stokes U map (bottom panel).

$$N \equiv \langle nn^\dagger \rangle_{\mathcal{P}(n)} \equiv \int \mathcal{D}n \langle nn^\dagger \rangle \mathcal{P}(n), \quad (3)$$

where the dagger denotes a transposed and complex conjugated quantity, $\mathcal{P}(s)$ and $\mathcal{P}(n)$ denote the probability density functions of signal and noise, respectively, and the integrals have to be taken over all pixels i , e.g.

$$\mathcal{D}s \equiv \prod_{i=1}^{N_{\text{pix}}} ds^i. \quad (4)$$

If we assume the signal prior and the noise distribution to be Gaussian, we obtain the signal posterior

$$\mathcal{P}(s | d) = \mathcal{G}(s - s_{\text{rec}}, D). \quad (5)$$

Here, we have defined

$$\mathcal{G}(\chi, C) \equiv \frac{1}{\sqrt{|2\pi C|}} \exp\left(-\frac{1}{2}\chi^\dagger C^{-1}\chi\right) \quad (6)$$

to denote the probability density function of a Gaussian distributed vector χ with zero mean, given the cosmological parameters p and the covariance matrix $C \equiv \langle \chi\chi^\dagger \rangle$, where the averages are taken over the Gaussian distribution $\mathcal{G}(\chi, C)$. In eq. (5), we have used the definitions

$$s_{\text{rec}} \equiv (S^{-1} + R^\dagger N^{-1}R)^{-1} R^\dagger N^{-1}d, \quad (7)$$

which is called the Wiener reconstruction of the signal, and

$$D \equiv (S^{-1} + R^\dagger N^{-1}R)^{-1}, \quad (8)$$

which denotes the Wiener variance with which the real signal, s , fluctuates around the reconstruction, s_{rec} . A detailed derivation of the posterior distribution, eq. (5), can for example be found in Enßlin et al. (2008) or in Frommert et al. (2008).

3 SPLITTING OF THE TEMPERATURE MAP

In this section, we split the WMAP temperature map into a part correlated with the WMAP polarization map, $T_{\text{corr}}^{\text{rec}}$, and a part which is not, $T_{\text{uncorr}}^{\text{rec}}$. This is the same splitting which has been done in Frommert & Enßlin (2009) in order to reduce the noise in ISW measurements. We translate the polarization map into the correlated part of the temperature map, using the cross-correlation between the two. However, as we already mentioned in the last section, before doing so we perform a Wiener filtering of the observed polarization map in order to reduce the noise.

Our data model for the observed polarization map P , which contains the Stokes Q and U maps shown in Fig. 1, is

$$P \equiv \begin{pmatrix} Q \\ U \end{pmatrix} \equiv W (P_{\text{cmb}} + P_{\text{det}} + P_{\text{fg}}). \quad (9)$$

Here, P_{cmb} is the intrinsic CMB polarization, P_{det} and P_{fg} denote the detector noise and residual foregrounds, respectively, and we have introduced the window W in order to describe the mask.

Let us define the signal covariance matrix of the CMB polarization given the cosmological parameters p ,

$$S_P \equiv \langle P_{\text{cmb}} P_{\text{cmb}}^\dagger \rangle_{\mathcal{P}(P_{\text{cmb}} | p)}, \quad (10)$$

and the noise covariance matrices for the detector noise and the residual foregrounds:

$$\begin{aligned} N_{\text{det}} &\equiv \langle P_{\text{det}} P_{\text{det}}^\dagger \rangle_{\mathcal{P}(P_{\text{det}})}, \\ N_{\text{fg}} &\equiv \langle P_{\text{fg}} P_{\text{fg}}^\dagger \rangle_{\mathcal{P}(P_{\text{fg}})}. \end{aligned} \quad (11)$$

The signal power spectrum (and thus S_P) has been computed using CMBEASY (Doran 2005) for the Maximum Likelihood cosmological model from Dunkley et al. (2009): $\{\Omega_b h^2 = 0.0227, \Omega_\Lambda = 0.751, H_0 = 0.724, \tau = 0.089, n_s = 0.961, \sigma_8 = 0.787\}$.

In order to derive the Wiener filter for P , let us define the noise,

$$n \equiv W (P_{\text{det}} + P_{\text{fg}}), \quad (12)$$

for which the noise covariance is then

$$N_P \equiv \langle n n^\dagger \rangle_{\mathcal{P}(n)} = W (N_{\text{det}} + N_{\text{fg}}) W^\dagger, \quad (13)$$

where we have assumed that P_{det} and P_{fg} are uncorrelated. We take the total noise covariance, N_P , for the observed polarization map from the WMAP code. We further identify P_{cmb} with the signal s , the mask W with the response R , and P with the data d . With these definitions, we have translated our data model, eq. (9), into the one given in eq. (1). If we assume the noise n and the signal P_{cmb} to be Gaussian distributed¹, we therefore obtain the posterior distribution for the signal

$$\mathcal{P}(P_{\text{cmb}} | P, p) = \mathcal{G}(P_{\text{cmb}} - P_{\text{cmb}}^{\text{rec}}, D_p), \quad (14)$$

with

$$P_{\text{cmb}}^{\text{rec}} \equiv (S_P^{-1} + W^\dagger N_P^{-1}W)^{-1} W^\dagger N_P^{-1}P, \quad (15)$$

which is the Wiener reconstruction of the polarization map, and

$$D_p \equiv (S_P^{-1} + W^\dagger N_P^{-1}W)^{-1}, \quad (16)$$

which denotes the Wiener variance. We show the Stokes Q and U maps of the Wiener filtered polarization map $P_{\text{cmb}}^{\text{rec}}$ in the top

¹ The assumption of Gaussianity holds well for the detector noise P_{det} and the signal P_{cmb} . For the residual galactic foregrounds, this assumption is probably less accurate.

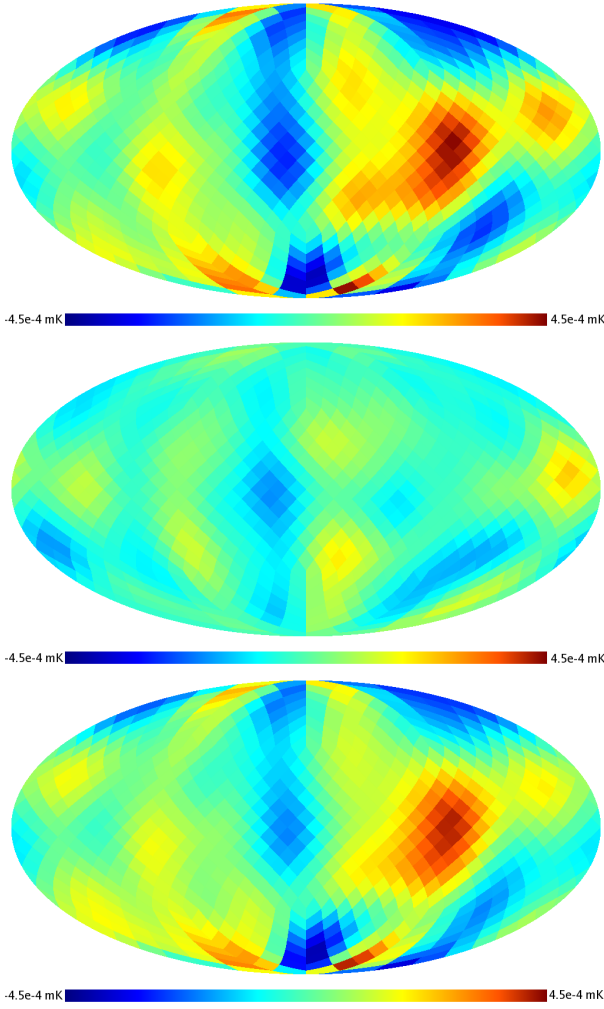


Figure 2. Stokes Q part of the following polarization maps: **Top panel:** Wiener filtered polarization map, $P_{\text{cmb}}^{\text{rec}}$. **Middle panel:** Part of the polarization map correlated with the temperature map, $P_{\text{corr}}^{\text{rec}}$. **Bottom panel:** Part of the polarization map uncorrelated with the temperature map, $P_{\text{uncorr}}^{\text{rec}}$. The colour scale is the same in all maps.

panels of Fig. 2 and Fig. 3, respectively. Note that only the low l modes survive the Wiener filtering, whereas the higher l modes are strongly suppressed due to the high noise-level they contain.

We now split the WMAP temperature map into a part correlated with the polarization map, $T_{\text{corr}}^{\text{rec}}$, and a part uncorrelated with the latter, $T_{\text{uncorr}}^{\text{rec}}$. We use the Wiener filtered polarization map $P_{\text{cmb}}^{\text{rec}}$, which is of resolution NSIDE=8, and the internal linear combination (ILC) temperature map (Gold et al. 2009), which we have smoothed with a Gaussian beam of FWHM=18.3° and downgraded to the same resolution. Among the different WMAP temperature maps, the ILC is the one for which the alignment of the low multipoles is least contaminated by galactic foregrounds (Gruppuso & Burigana 2009). When working on large scales, we can safely neglect the detector noise in the temperature data (Afshordi 2004). Furthermore, we decide to neglect residual foregrounds in the temperature map.

We translate the Wiener filtered polarization map, $P_{\text{cmb}}^{\text{rec}}$, into the correlated part of the temperature map, using the cross-correlation between the two:

$$T_{\text{corr}}^{\text{rec}} \equiv S_{T,P} S_P^{-1} P_{\text{cmb}}^{\text{rec}}, \quad (17)$$

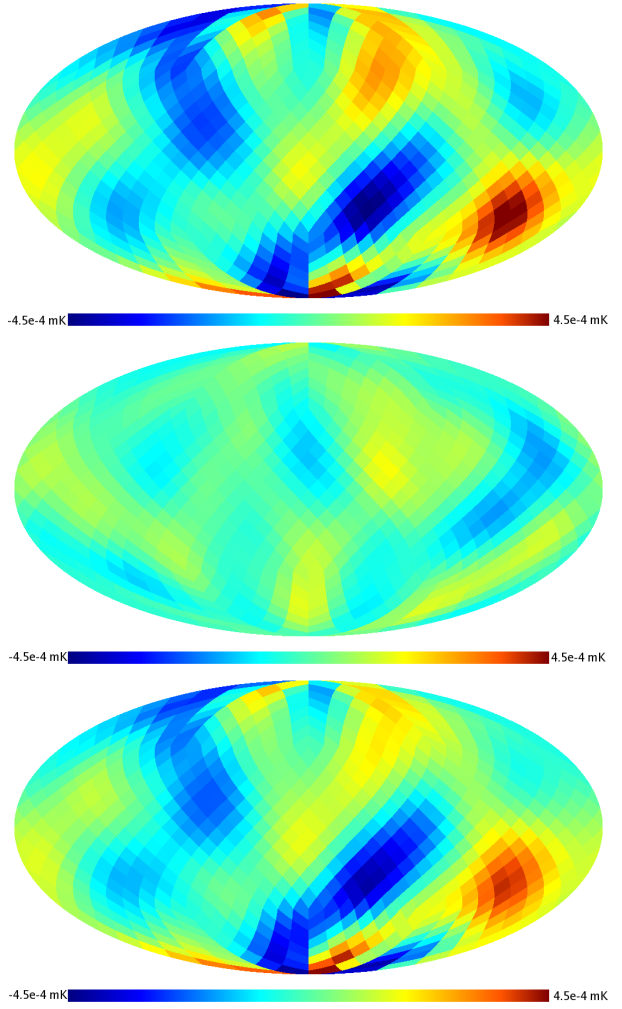


Figure 3. Stokes U part of the following polarization maps: **Top panel:** Wiener filtered polarization map, $P_{\text{cmb}}^{\text{rec}}$. **Middle panel:** Part of the polarization map correlated with the temperature map, $P_{\text{corr}}^{\text{rec}}$. **Bottom panel:** Part of the polarization map uncorrelated with the temperature map, $P_{\text{uncorr}}^{\text{rec}}$. The colour scale is the same in all maps.

where the signal covariance matrices given the cosmological parameters, p , are defined as

$$S_{P,T} \equiv \langle P_{\text{cmb}} T^\dagger \rangle_{\mathcal{P}(T, P_{\text{cmb}} | p)}, \quad (18)$$

$$S_T \equiv \langle T T^\dagger \rangle_{\mathcal{P}(T | p)}. \quad (19)$$

The uncorrelated temperature map $T_{\text{uncorr}}^{\text{rec}}$ is then obtained by simply subtracting $T_{\text{corr}}^{\text{rec}}$ from T :

$$T_{\text{uncorr}}^{\text{rec}} \equiv T - T_{\text{corr}}^{\text{rec}}. \quad (20)$$

In Appendix A, we prove that $T_{\text{corr}}^{\text{rec}}$ and $T_{\text{uncorr}}^{\text{rec}}$ are indeed uncorrelated.

We plot T , $T_{\text{corr}}^{\text{rec}}$, and $T_{\text{uncorr}}^{\text{rec}}$ in the top, middle, and bottom panel of Fig. 4, respectively. Let us first concentrate on $T_{\text{corr}}^{\text{rec}}$, and try to assess whether some of its structures could come from galactic foregrounds rather than being intrinsic CMB fluctuations. Comparing $T_{\text{corr}}^{\text{rec}}$ with the overview over the galactic foregrounds published in Hinshaw et al. (2007), Fig. 7, makes us suspect that the warm region in the middle of the northern hemisphere might be associated with the north galactic spur. A part of this region is already masked out, but it is well possible that the mask should be bigger in

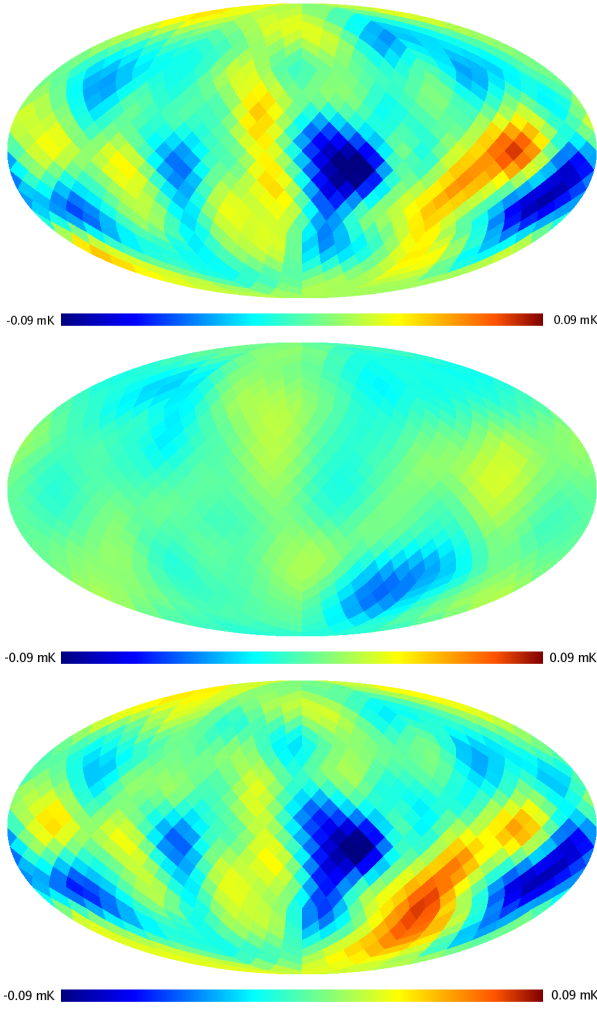


Figure 4. **Top panel:** ILC map, smoothed with a beam of 18.3° and downgraded to a resolution of $\text{NSIDE}=8$. **Middle panel:** Part of the temperature map which is correlated with the polarization map, $T_{\text{CORR}}^{\text{rec}}$. **Bottom panel:** Part of the temperature map which is uncorrelated with the polarization map, $T_{\text{UNCORR}}^{\text{rec}}$. The colour scale is the same in all maps.

order to better mask out this foreground. One might also think that the big red blob on the right hand side of $T_{\text{CORR}}^{\text{rec}}$, close to the galactic plane, could be due to the Gum Nebula. However, plotting the two maps on top of each other reveals that the Gum Nebula lies further to the East than our red blob. Therefore we exclude that the blob comes from that particular foreground.

Let us now compare the three maps T , $T_{\text{CORR}}^{\text{rec}}$, and $T_{\text{UNCORR}}^{\text{rec}}$. In the northern galactic hemisphere, all maps look quite similar, apart from the hot region around the north galactic spur, which is more prominent in $T_{\text{CORR}}^{\text{rec}}$ than in the other two maps, and which we have already commented on. However, in the western part of the southern hemisphere, we obtain a strong deviation of $T_{\text{CORR}}^{\text{rec}}$ from the ILC map. In fact, the features in $T_{\text{CORR}}^{\text{rec}}$ have the opposite sign to the structures in the ILC map. This enhances the amplitudes of the features in the western part of the southern hemisphere in $T_{\text{UNCORR}}^{\text{rec}}$ as compared to the ILC map. In particular, the so-called *cold spot*, which has been found to have non-Gaussian characteristics by Vielva et al. (2004), turns out to be even colder in $T_{\text{UNCORR}}^{\text{rec}}$ than in the ILC map. The cold spot, which we mark in the ILC map in Fig. 5 by a black circle, has later been confirmed to have non-Gaussian characteris-

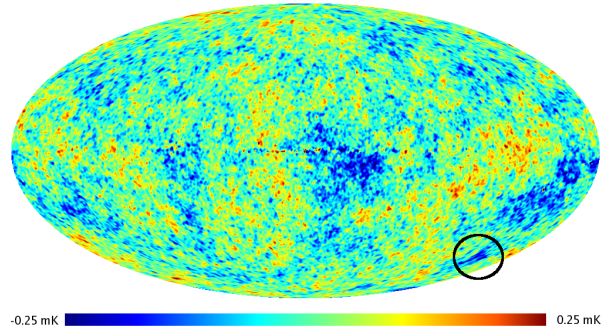


Figure 5. The *cold spot*, which has been found to have non-Gaussian characteristics, is marked in the ILC map shown here by a black circle.

tics by many others (see, e.g., Martínez-González et al. 2006; Cruz et al. 2006; Naselsky et al. 2007). It would be interesting to redo the above-mentioned analyses of the cold spot with the high-resolution version of $T_{\text{UNCORR}}^{\text{rec}}$, in order to see whether the significance of the non-Gaussian features is even higher in that map. A thorough analysis of the characteristics of the cold spot is beyond the scope of this work, though, and we leave this exciting question for future work. Lastly, we notice that on the large scales we are looking at, we have much stronger deviations of the temperature towards the cold end of the temperature spectrum than towards the warm end, for all three of the maps.

4 SPLITTING OF THE POLARIZATION MAP

We now split the WMAP polarization map into a part correlated with the WMAP temperature map, P_{CORR} , and a part uncorrelated with that, P_{UNCORR} . As before, we obtain the correlated polarization map by simply translating the temperature map into a polarization map:

$$P_{\text{CORR}} \equiv S_{P,T} S_T^{-1} T, \quad (21)$$

The Stokes Q and U maps of P_{CORR} are shown in the middle panels of Fig. 2 and Fig. 3, respectively.

In order to obtain the uncorrelated map, we would like to subtract P_{CORR} from P_{CMB} :

$$P_{\text{UNCORR}} \equiv P_{\text{CMB}} - P_{\text{CORR}}. \quad (22)$$

However, we do not know P_{CMB} because we only observe P , which is highly contaminated by noise. Subtracting P_{CORR} from the Wiener filtered polarization map, $P_{\text{CMB}}^{\text{rec}}$, does not result in uncorrelated maps. We therefore subtract $W P_{\text{CORR}}$ from the observed polarization map, P :

$$\begin{aligned} P_{\text{UNCORR}}^{\text{raw}} &\equiv P - W P_{\text{CORR}} \\ &= W P_{\text{UNCORR}} + n, \end{aligned} \quad (23)$$

where the noise n is the same as in section 3. We then compute the Wiener reconstruction of the signal P_{UNCORR} , with the data being $P_{\text{UNCORR}}^{\text{raw}}$:

$$P_{\text{UNCORR}}^{\text{rec}} = [(S_P - S_{P,T} S_T^{-1} S_{T,P})^{-1} + W^\dagger N_P^{-1} W]^{-1} W^\dagger N_P^{-1} P_{\text{UNCORR}}^{\text{raw}}. \quad (24)$$

Here, we have used the signal covariance

$$\begin{aligned} &\langle P_{\text{UNCORR}} P_{\text{UNCORR}}^\dagger \rangle_{\mathcal{P}(P_{\text{CMB}}, T | P)} \\ &= \langle P_{\text{CMB}} P_{\text{CMB}}^\dagger \rangle - \langle P_{\text{CMB}} T^\dagger \rangle S_T^{-1} S_{T,P} \end{aligned}$$

$$\begin{aligned}
& -S_{P,T}S_T^{-1}\langle TP_{\text{cmb}}^\dagger \rangle + S_{P,T}S_T^{-1}\langle TT^\dagger \rangle S_T^{-1}S_{T,P} \\
& = S_P - S_{P,T}S_T^{-1}S_{T,P}. \quad (25)
\end{aligned}$$

$P_{\text{uncorr}}^{\text{rec}}$ given in eq. (24) is uncorrelated with P_{corr} , as we prove in Appendix B. The posterior of P_{uncorr} is given by

$$\mathcal{P}(P_{\text{uncorr}} | T, P, p) = \mathcal{G}(P_{\text{uncorr}} - P_{\text{uncorr}}^{\text{rec}}, D_{\text{uncorr}}), \quad (26)$$

with the Wiener variance

$$D_{\text{uncorr}} \equiv [(S_P - S_{P,T}S_T^{-1}S_{T,P})^{-1} + W^\dagger N_P^{-1}W]^{-1}. \quad (27)$$

We show the Stokes Q and U maps of the uncorrelated polarization map, $P_{\text{uncorr}}^{\text{rec}}$, in the bottom panels of Fig. 2 and Fig. 3, respectively. Note that the symbols for the correlated and uncorrelated parts of temperature and polarization maps are listed and briefly explained in table 1.

5 THE AXIS OF EVIL

We now search for the axis of evil in the four maps P_{corr} , $P_{\text{uncorr}}^{\text{rec}}$, $T_{\text{corr}}^{\text{rec}}$, and $T_{\text{uncorr}}^{\text{rec}}$. Note that P_{corr} and $T_{\text{corr}}^{\text{rec}}$ have of course the same axes as the original temperature and polarization maps, T and $P_{\text{cmb}}^{\text{rec}}$, respectively. To define the preferred axis, we use a statistic proposed by de Oliveira-Costa et al. (2004), which has been introduced in order to quantify the preferred direction that can be picked out in the smoothed temperature map by eye. When looking at the smoothed ILC map in Fig. 4, most of the hot and cold blobs seem to be lying on the same plane. The quadrupole and octopole extracted from the ILC map show the same behaviour (see, e.g., de Oliveira-Costa et al. 2004), and the planes are roughly the same for the two multipoles. In order to quantify this alignment, de Oliveira-Costa et al. (2004) came up with the following statistic. The temperature maps are expanded into spherical harmonics, which are eigenfunctions of the square and the z-component of the angular momentum operator L :

$$T(\hat{n}) = \sum_l T_l(\hat{n}) \equiv \sum_{l,m} a_{lm}^T Y_{lm}(\hat{n}). \quad (28)$$

Then, for every multipole l , one determines the z-axis \hat{n} for which the expectation value of the z-component of L , $\hat{n} \cdot L$, is maximised:

$$\langle T_l | (\hat{n} \cdot L)^2 | T_l \rangle = \sum_m m^2 | a_{lm}(\hat{n}) |^2, \quad (29)$$

Here, $a_{lm}(\hat{n})$ denotes the spherical harmonic coefficient a_{lm} obtained in a coordinate system with the z-axis pointing in \hat{n} -direction. We determine the axis \hat{n} by simply rotating the z-axis into every pixel centre and checking for the maximum, which is well feasible at our resolution. Neighbouring pixel centres in our map differ by approximately 7° , but we will soon see that the uncertainties in our axes are so large that it is sufficient to check only the pixel centres as potential z-axes. We have done the same exercise allowing the axes to point to all pixel centres of NSIDE=16 instead of NSIDE=8, and our results are robust under this change.

As we have already mentioned, the mask, residual foregrounds and detector noise in the polarization data will result in an uncertainty in the preferred axes. The posterior distribution of the real CMB polarization map, P_{cmb} , given the one we observe, P , is given by eq. (14). P_{cmb} fluctuates around our Wiener reconstruction, $P_{\text{cmb}}^{\text{rec}}$, with the Wiener variance D_P .

In order to obtain the uncertainties in the axes of $T_{\text{corr}}^{\text{rec}}$ and $T_{\text{uncorr}}^{\text{rec}}$, we have run Monte Carlo (MC) simulations, drawing realisations of P_{cmb} from its posterior distribution. From these, we

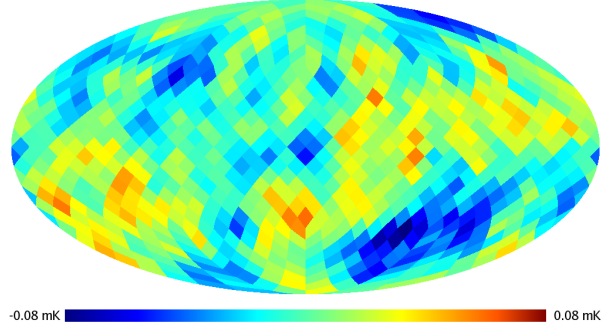


Figure 6. Wiener realisation of T_{corr}

obtain realisations of

$$\begin{aligned}
T_{\text{corr}} & \equiv S_{T,P} S_P^{-1} P_{\text{cmb}}, \\
T_{\text{uncorr}} & \equiv T - T_{\text{corr}}, \quad (30)
\end{aligned}$$

for which we then determine the preferred axes. The uncertainty in the axes of $P_{\text{uncorr}}^{\text{rec}}$ is obtained similarly, using the posterior distribution of P_{uncorr} given in eq. (26). Note that T and thus P_{corr} are assumed to have no contributions from residual foregrounds or detector noise, and thus no uncertainty in the preferred axes.

For drawing realisations from the probability distribution in eq. (14), we have computed the Wiener variance D_P given in eq. (16). We have then computed the Cholesky factorisation L of D_P , which is a particular form of the square-root of a positive definite matrix:

$$D_P = LL^\dagger. \quad (31)$$

In order to obtain our realisation, P_{cmb} , we apply L to a map n_w of white noise, i.e. a map where the temperature at every pixel is independently drawn from a Gaussian distribution with unit variance, and add the mean value $P_{\text{cmb}}^{\text{rec}}$: $P_{\text{cmb}} \equiv L n_w + P_{\text{cmb}}^{\text{rec}}$. This results in a map which is drawn from the distribution in eq. (14), as one can easily see:

$$\begin{aligned}
& \langle (P_{\text{cmb}} - P_{\text{cmb}}^{\text{rec}})(P_{\text{cmb}} - P_{\text{cmb}}^{\text{rec}})^\dagger \rangle_{\mathcal{P}(n_w)} \\
& = L \langle n_w n_w^\dagger \rangle_{\mathcal{P}(n_w)} L^\dagger = LL^\dagger = D_P. \quad (32)
\end{aligned}$$

An example of a Wiener realisation of T_{corr} is shown in Fig. 6.²

We plot the axes and their uncertainties for the different maps in Figs 7-10. Both ends of every axis are marked by a cross in the maps, and the colour coding counts how many times the preferred axis came to lie on the respective pixels in 5000 MC samples.

All axes and their standard deviations σ , which we obtained from the MC simulations, are summarised in table 1. For P_{corr} , and thus the ILC map, we reproduce the results from de Oliveira-Costa et al. (2004) within our measurement precision: the axes of the quadrupole and the octopole of P_{corr} point in the same direction, which is roughly $(l, b) \approx (-120^\circ, 63^\circ)$, where l and b denote galactic longitude and latitude, respectively (de Oliveira-Costa et al. (2004) found $(l, b) \approx (-110^\circ, 60^\circ)$). For $T_{\text{uncorr}}^{\text{rec}}$, again both

² We had to regularise the Wiener variances, eqs (16) and (27), by adding Gaussian noise in order to make them positive definite. This is required by the Cholesky factorisation. However, since the noise was added mostly on small scales, the quadrupole and octopole remained completely unaffected by this. In fact, our results remained unchanged under varying the variance of the added Gaussian noise over 5 orders of magnitude.

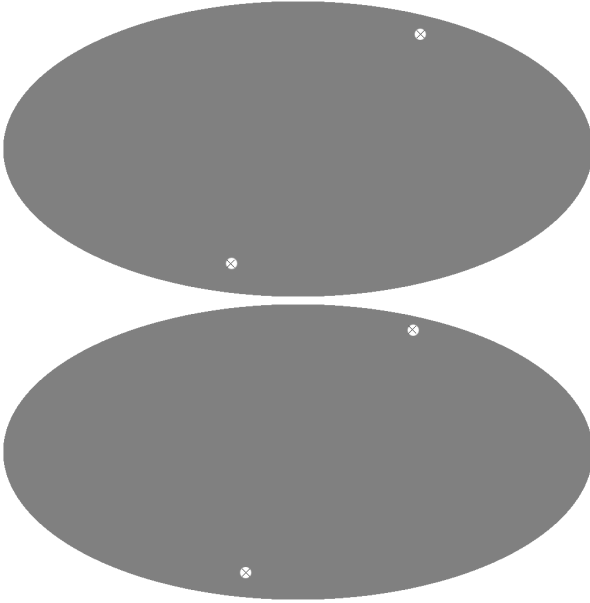


Figure 7. Preferred axis of the quadrupole (top panel) and the octopole (bottom panel) for P_{corr} and thus for the ILC map. We reproduce the results of de Oliveira-Costa et al. (2004) within our measurement precision. The axes of quadrupole and octopole point in the same direction, which has been named the axis of evil.

axes point in the same direction as the axes of P_{corr} within our measurement precision.

For $P_{\text{uncorr}}^{\text{rec}}$, the preferred axis of the quadrupole has an angular distance to the average axis of the ILC map of 37° . That means that the latter lies inside its 1σ region. The same holds for $T_{\text{corr}}^{\text{rec}}$ (and thus $P_{\text{cmb}}^{\text{rec}}$), for which the axis of the quadrupole has an angular distance to the average axis of the ILC map of 34° . The axes of the octopole of $P_{\text{uncorr}}^{\text{rec}}$ and $T_{\text{corr}}^{\text{rec}}$, though, do not align with the axis of evil. What can we learn from this result? The significance of the alignment between the axes of the quadrupole and octopole in the temperature map has been assessed extensively in earlier works. In this work, we only look at the additional information we obtain from the axes of $P_{\text{uncorr}}^{\text{rec}}$. To this end, let us take the preferred axis in the temperature map T as given, and assume that the axes of $P_{\text{uncorr}}^{\text{rec}}$ are distributed isotropically over the sky and independently from each other. In Appendix C, we work out the probability for at least one of the axes of $P_{\text{uncorr}}^{\text{rec}}$ being such that the axis of the temperature map is included in the 1σ region around it. This probability amounts to about 50 per cent, due to the large 1σ regions we have.

In order to assess whether the mask or the noise in the WMAP polarization maps is the main source of uncertainty in the axes, we have determined the uncertainty with the amplitude of the noise covariance matrix rescaled to 10 per cent of the original one. This yields an uncertainty of about 20° in the axes. We have done the same exercise for the noise amplitude downscaled to 1 per cent of the original one, which results in an uncertainty of $7^\circ - 10^\circ$ in the axes. This means that the noise is actually the main source of uncertainty in our analysis rather than the mask. Soon, the *Planck* surveyor mission (Tauber 2000) will provide us with polarization measurements that have a noise-level which is significantly below the one in the WMAP data. The main problem will then be the contamination of the polarization data by galactic foregrounds. In the WMAP polarization data, the foregrounds contribute about 20 per cent to the diagonal of the noise covariance matrix N_P in pixel

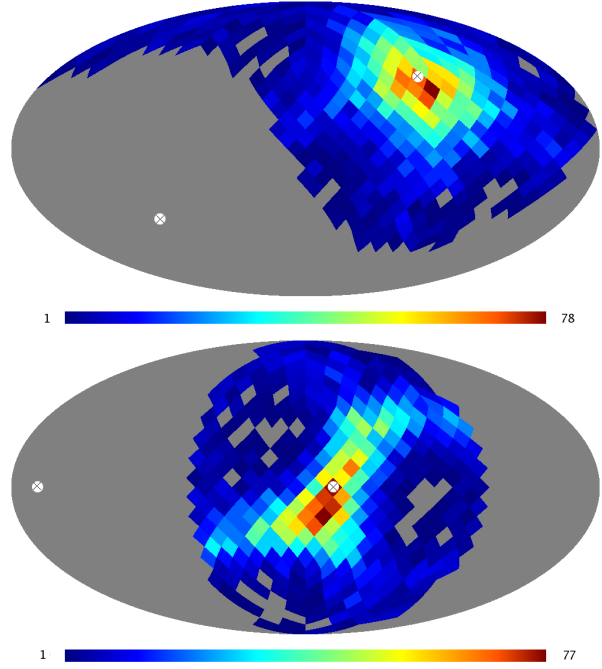


Figure 8. Preferred axis of the quadrupole (top panel) and the octopole (bottom panel) for $P_{\text{uncorr}}^{\text{rec}}$. The colour coding counts the number of MC samples whose axis came to lie on the respective pixel. The axis of the quadrupole aligns with the axis of evil within our measurement precision, whereas the axis of the octopole does not.

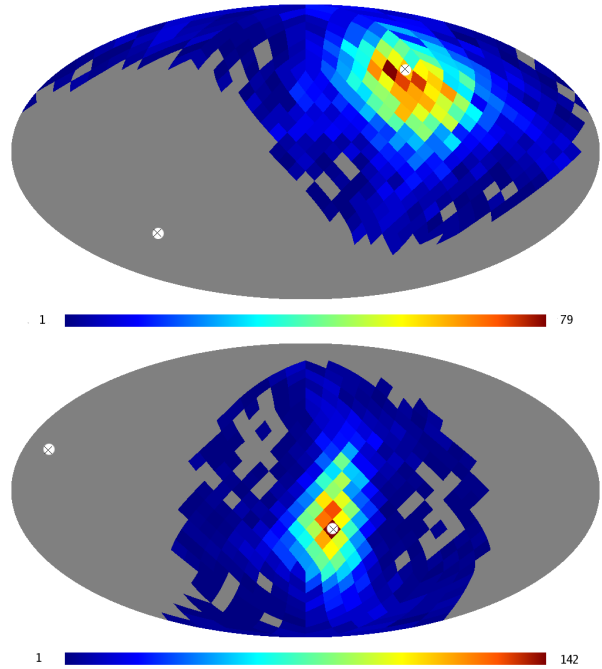


Figure 9. Preferred axis of the quadrupole (top panel) and the octopole (bottom panel) for $T_{\text{corr}}^{\text{rec}}$ and thus for $P_{\text{cmb}}^{\text{rec}}$. The axis of the quadrupole aligns with the axis of evil within our measurement precision, whereas the axis of the octopole does not.

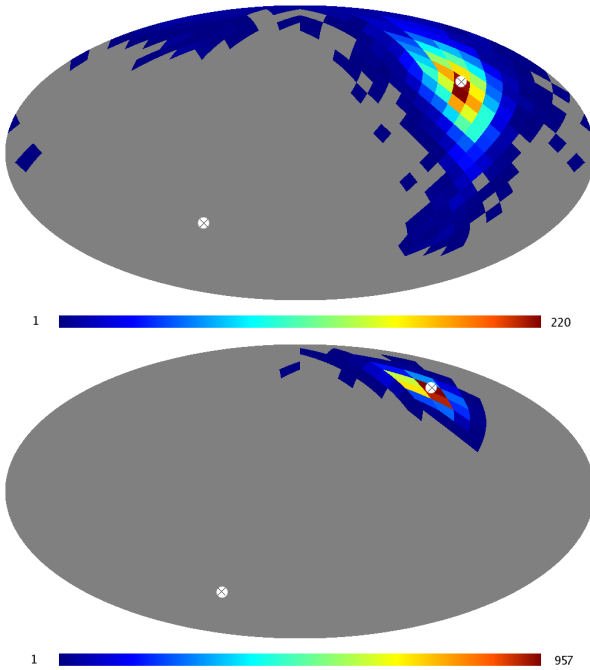


Figure 10. Preferred axis of the quadrupole (top panel) and the octopole (bottom panel) for $T_{\text{uncorr}}^{\text{rec}}$. The axes of the quadrupole and the octopole both align with the axis of evil within our measurement precision.

space. With *Planck*, we will be able to determine the foregrounds better than with WMAP, due to the broader frequency range covered by *Planck*. If we assume that the covariance due to residual foregrounds for *Planck* will be between 5 and 50 per cent of the one for WMAP, we will get the uncertainty on the axes down to about 10° and 20° , respectively. With this, we will have a powerful test to probe the axis of evil in polarization.

6 CONCLUSIONS

In the last few years, a preferred axis has been found in the CMB temperature map, posing a challenge to the cosmological principle. This so-called *axis of evil* denotes the unusual alignment of the preferred axes of the quadrupole and the octopole in the temperature map.

In this work, we have split the CMB temperature and polarization maps from WMAP into a part correlated with the respective other map, and an uncorrelated part. If the axis of evil were due to some preferred direction intrinsic to our Universe, we would expect its signature to be present in all four of these maps. In particular, the part of the polarization map which is uncorrelated with the temperature map serves as an independent probe of the axis of evil.

In order to reduce the noise contained in the polarization maps, we have Wiener filtered the maps before computing the preferred axes. We have then determined the preferred axes of the quadrupole and the octopole for the four maps. In order to assess the uncertainty in the axes coming from the mask, detector noise and residual foregrounds in the polarization maps, we have run MC simulations conditional on the observational data.

For the part of the polarization map which is correlated with the temperature map, P_{corr} , we find that the axes of quadrupole and octopole point in the same direction, confirming earlier results by de Oliveira-Costa et al. (2004). The part of the temperature map

which is uncorrelated with the polarization map, $T_{\text{uncorr}}^{\text{rec}}$, exhibits the same alignment of the axes within our measurement precision.

For the part of the polarization map which is uncorrelated with the temperature map, $P_{\text{uncorr}}^{\text{rec}}$, we find that only the axis of the quadrupole aligns with the axis of evil, whereas the axis of the octopole does not. The same holds for the correlated part of the temperature map, $T_{\text{corr}}^{\text{rec}}$. We have computed the probability that a rough alignment with the axis of evil, as we find it for the axis of the quadrupole of $P_{\text{uncorr}}^{\text{rec}}$, happens by chance if the axes are distributed isotropically. This probability amounts to 50 per cent for currently available polarization data, due to the large uncertainties in the axes. We are thus looking forward to redoing this analysis with polarization maps from *Planck*, which will yield much more significant results.

ACKNOWLEDGEMENTS

The authors would like to thank Simon White for a suggestion that greatly improved this paper. We further thank Thomas Riller, Carlos Hernandez-Monteagudo, Christoph R ath, and Anthony Banday for useful discussions and comments; Martin Reinecke, Mariapaola Bottino, and Andr e Waelkens for their help with HEALPix, and Claudia Scoccola for reading the manuscript. We acknowledge the use of the HEALPix package (Gorski et al. 2005), the *Legacy Archive for Microwave Background Data Analysis* (LAMBDA), and CMBEASY (Doran 2005).

REFERENCES

- Abramo L. R., Bernui A., Ferreira I. S., Villela T., Wuensche C. A., 2006, *Phys. Rev. D*, 74, 063506
- Afshordi N., 2004, *Phys. Rev. D*, 70, 083536
- Basak S., Hajian A., Souradeep T., 2006, *Phys. Rev. D*, 74, 021301
- Bernui A., 2008, *Phys. Rev. D*, 78, 063531
- Cruz M., Tucci M., Mart nez-Gonz alez E., Vielva P., 2006, *MNRAS*, 369, 57
- de Oliveira-Costa A., Tegmark M., Zaldarriaga M., Hamilton A., 2004, *Phys. Rev. D*, 69, 063516
- Dolag K., Hansen F. K., Roncarelli M., Moscardini L., 2005, *MNRAS*, 363, 29
- Doran M., 2005, *Journal of Cosmology and Astro-Particle Physics*, 10, 11
- Dunkley J., Komatsu E., Nolta M. R., Spergel D. N., Larson D., Hinshaw G., Page L., Bennett C. L., Gold B., Jarosik N., Weiland J. L., Halpern M., Hill R. S., Kogut A., Limon M., Meyer S. S., Tucker G. S., Wollack E., Wright E. L., 2009, *ApJS*, 180, 306
- Dvorkin C., Peiris H. V., Hu W., 2008, *Phys. Rev. D*, 77, 063008
- En ßlin T. A., Frommert M., Kitaura F. S., 2008, submitted to *Phys. Rev. D*
- Eriksen H. K., Banday A. J., Gorski K. M., Hansen F. K., Lilje P. B., 2007, *ApJ*, 660, L81
- Frommert M., En ßlin T. A., 2009, *MNRAS*, 395, 1837
- Frommert M., En ßlin T. A., Kitaura F. S., 2008, *MNRAS*, 391, 1315
- Gold B., Bennett C. L., Hill R. S., Hinshaw G., Odegard N., Page L., Spergel D. N., Weiland J. L., Dunkley J., Halpern M., Jarosik N., Kogut A., Komatsu E., Larson D., Meyer S. S., Nolta M. R., Wollack E., Wright E. L., 2009, *ApJS*, 180, 265

- Górski K. M., Hivon E., Banday A. J., Wandelt B. D., Hansen F. K., Reinecke M., Bartelmann M., 2005, *ApJ*, 622, 759
- Groeneboom N. E., Eriksen H. K., 2009, *ApJ*, 690, 1807
- Gruppuso A., Burigana C., 2009, *ArXiv e-prints*
- Hinshaw G., et al., 2007, *ApJS*, 170, 288
- Hinshaw G., et al., 2009, *ApJS*, 180, 225
- Hoftuft J., Eriksen H. K., Banday A. J., Górski K. M., Hansen F. K., Lilje P. B., 2009, *ApJ*, 699, 985
- Inoue K. T., Silk J., 2007, *ApJ*, 664, 650
- Land K., Magueijo J., 2007, *MNRAS*, 378, 153
- Magueijo J., Sorkin R. D., 2007, *MNRAS*, 377, L39
- Martínez-González E., Cruz M., Cayón L., Vielva P., 2006, *New Astronomy Review*, 50, 875
- Maturi M., Dolag K., Waelkens A., Springel V., Enßlin T., 2007, *A&A*, 476, 83
- Morales J. A., Sáez D., 2008, *ApJ*, 678, 583
- Naselsky P. D., Christensen P. R., Coles P., Verkhodanov O., Novikov D., Kim J., 2007, *ArXiv e-prints*
- Page L., et al., 2007, *ApJS*, 170, 335
- Rakić A., Schwarz D. J., 2007, *Phys. Rev. D*, 75, 103002
- Samal P. K., Saha R., Jain P., Ralston J. P., 2008, *MNRAS*, 385, 1718
- Samal P. K., Saha R., Jain P., Ralston J. P., 2009, *MNRAS*, 396, 511
- Souradeep T., Hajian A., Basak S., 2006, *New Astronomy Review*, 50, 889
- Tauber J. A., 2000, *Astrophysical Letters Communications*, 37, 145
- Vielva P., Martínez-González E., Barreiro R. B., Sanz J. L., Cayón L., 2004, *ApJ*, 609, 22
- Vielva P., Wiaux Y., Martínez-González E., Vanderghelynst P., 2007, *MNRAS*, 381, 932

APPENDIX A: PROOF OF VANISHING CORRELATION BETWEEN $T_{\text{corr}}^{\text{rec}}$ AND $T_{\text{uncorr}}^{\text{rec}}$

We now prove that the two maps $T_{\text{corr}}^{\text{rec}}$ and $T_{\text{uncorr}}^{\text{rec}}$, into which we split the temperature map T in section 3, are indeed uncorrelated. To this end, let us write

$$\begin{aligned}
 T_{\text{corr}}^{\text{rec}} &= S_{T,P} S_P^{-1} P_{\text{cmb}}^{\text{rec}} \\
 &= S_{T,P} S_P^{-1} (S_P^{-1} + W^\dagger N_P^{-1} W)^{-1} W^\dagger N_P^{-1} P \\
 &= S_{T,P} (1 + W^\dagger N_P^{-1} W S_P)^{-1} W^\dagger N_P^{-1} P \\
 &= S_{T,P} W^\dagger (1 + N_P^{-1} W S_P W^\dagger)^{-1} N_P^{-1} P \\
 &= S_{T,P} W^\dagger (N_P + W S_P W^\dagger)^{-1} P, \tag{A1}
 \end{aligned}$$

where we have inserted $P_{\text{cmb}}^{\text{rec}}$ from eq. (15) in the first step. The third step can be easily verified by using the geometric series for $(1 + W^\dagger N_P^{-1} W S_P)^{-1} W^\dagger$, which has a convergence radius of 1, and is thus valid for $|W^\dagger N_P^{-1} W S_P| < 1$. In our case, this holds because our polarization data are noise-dominated.³

We will soon see that we need the following covariance matrices in the derivation:

$$\langle P P^\dagger \rangle_{\mathcal{P}(P|p)} = W S_P W^\dagger + N_P, \tag{A2}$$

³ By adding a small ϵ -term to the response W , and thus making it invertible, the third step also holds generally.

where we have assumed that P_{cmb} is uncorrelated with P_{det} and P_{fg} , and we have inserted the definition of N_P , eq. (13).

Since we neglect the detector noise and residual foregrounds in the temperature data, we obtain for the covariance between temperature and polarization data

$$\begin{aligned}
 \langle T P^\dagger \rangle_{\mathcal{P}(T,P|p)} &= \langle T P_{\text{cmb}}^\dagger \rangle_{\mathcal{P}(T,P_{\text{cmb}}|p)} W^\dagger \\
 &\equiv S_{T,P} W^\dagger, \tag{A3}
 \end{aligned}$$

where we have assumed that detector noise and residual foregrounds in the polarization map are uncorrelated with the CMB temperature map.

Let us now look at

$$\begin{aligned}
 &\langle T_{\text{uncorr}}^{\text{rec}} T_{\text{corr}}^{\text{rec} \dagger} \rangle_{\mathcal{P}(T,P|p)} \\
 &= \langle T T_{\text{corr}}^{\text{rec} \dagger} \rangle_{\mathcal{P}(T,P|p)} - \langle T_{\text{corr}}^{\text{rec}} T_{\text{corr}}^{\text{rec} \dagger} \rangle_{\mathcal{P}(T,P|p)} \\
 &= \langle T P^\dagger \rangle_{\mathcal{P}(T,P|p)} (N_P + W S_P W^\dagger)^{-1} W S_{P,T} \\
 &\quad - S_{T,P} W^\dagger (N_P + W S_P W^\dagger)^{-1} \langle P P^\dagger \rangle_{\mathcal{P}(P|p)} \\
 &\quad (N_P + W S_P W^\dagger)^{-1} W S_{P,T} \\
 &= S_{T,P} W^\dagger (N_P + W S_P W^\dagger)^{-1} W S_{P,T} \\
 &\quad - S_{T,P} W^\dagger (N_P + W S_P W^\dagger)^{-1} (N_P + W S_P W^\dagger)^{-1} \\
 &\quad (N_P + W S_P W^\dagger)^{-1} W S_{P,T} \\
 &= S_{T,P} W^\dagger (N_P + W S_P W^\dagger)^{-1} W S_{P,T} \\
 &\quad - S_{T,P} W^\dagger (N_P + W S_P W^\dagger)^{-1} W S_{P,T} \\
 &= 0,
 \end{aligned}$$

where we have inserted eqs (A1), (A2), and (A3). QED

APPENDIX B: PROOF OF VANISHING CORRELATION BETWEEN P_{corr} AND $P_{\text{uncorr}}^{\text{rec}}$

For the splitting of the polarization map, we first prove that the unfiltered uncorrelated map defined in eq. (23), $P_{\text{uncorr}}^{\text{raw}}$, is uncorrelated with P_{corr} :

$$\begin{aligned}
 &\langle P_{\text{uncorr}}^{\text{raw}} P_{\text{corr}}^\dagger \rangle_{\mathcal{P}(T,P|p)} \\
 &= \langle P P_{\text{corr}}^\dagger \rangle_{\mathcal{P}(T,P|p)} - W \langle P_{\text{corr}} P_{\text{corr}}^\dagger \rangle_{\mathcal{P}(T,P|p)} \\
 &= \langle P T^\dagger \rangle_{\mathcal{P}(T,P|p)} S_T^{-1} S_{T,P} \\
 &\quad - W S_{P,T} S_T^{-1} \langle T T^\dagger \rangle_{\mathcal{P}(T,P|p)} S_T^{-1} S_{T,P} \\
 &= W S_{P,T} S_T^{-1} S_{T,P} - W S_{P,T} S_T^{-1} S_T S_T^{-1} S_{T,P} \\
 &= W S_{P,T} S_T^{-1} S_{T,P} - W S_{P,T} S_T^{-1} S_{T,P} \\
 &= 0. \tag{B1}
 \end{aligned}$$

From the above, we readily obtain that also the Wiener filtered uncorrelated map,

$$P_{\text{uncorr}}^{\text{rec}} = [(S_P - S_{P,T} S_T^{-1} S_{T,P})^{-1} + W^\dagger N_P^{-1} W]^{-1} W^\dagger N_P^{-1} P_{\text{uncorr}}^{\text{raw}},$$

is uncorrelated with P_{corr} :

$$\begin{aligned}
 &\langle P_{\text{uncorr}}^{\text{rec}} P_{\text{corr}}^\dagger \rangle_{\mathcal{P}(T,P|p)} \\
 &= [(S_P - S_{P,T} S_T^{-1} S_{T,P})^{-1} + W^\dagger N_P^{-1} W]^{-1} \\
 &\quad W^\dagger N_P^{-1} \langle P_{\text{uncorr}}^{\text{raw}} P_{\text{corr}}^\dagger \rangle_{\mathcal{P}(T,P|p)} \\
 &= 0 \tag{B2}
 \end{aligned}$$

QED

APPENDIX C: PROBABILITY FOR CHANCE ALIGNMENT IN AN ISOTROPIC UNIVERSE

We would like to assess whether the rough alignment of the axis of the quadrupole in $P_{\text{uncorr}}^{\text{rec}}$ actually provides us with some information about the axis of evil. We therefore compute the probability for at least one of the axes of $P_{\text{uncorr}}^{\text{rec}}$ aligning with the axis of the temperature map in an isotropic Universe. To this end, let us take the preferred axis in the temperature map T as given, and assume that the axes of $P_{\text{uncorr}}^{\text{rec}}$ are distributed isotropically over the sky and independently from each other. We then work out the probability for at least one of the axes of $P_{\text{uncorr}}^{\text{rec}}$ being such that the axis of the temperature map is included in the 1σ region around it.

For simplicity, we assume that the 1σ regions are symmetric circles around the axes, with radius $\sigma \approx 45^\circ$ for both the quadrupole and the octopole. The solid angle A spanned by such a 1σ region is well approximated by $A \approx \pi\sigma^2$.⁴ The probability of at least one of the 1σ regions hitting the axis of evil is just the solid angle spanned by the two 1σ regions divided by the solid angle of the hemisphere, 2π . However, the solid angle spanned by the two 1σ regions depends on the overlap B between them, it is $2A - B$ to avoid double counting of the overlapping area. Given the angular separation α between the axes of the quadrupole and the octopole, the overlap can be computed as follows:

$$B(\alpha) = 2 \left[\sigma^2 \arccos\left(\frac{\alpha}{2\sigma}\right) - \frac{\alpha}{2} \sqrt{\sigma^2 - \frac{\alpha^2}{4}} \right], \quad (\text{C1})$$

which can be derived from the geometry of the problem in flat-sky approximation. We marginalise the hitting probability over the overlap $B(\alpha)$, using the fact that α is distributed as $\mathcal{P}(\alpha) = \sin(\alpha)$ (de Oliveira-Costa et al. 2004):

$$\begin{aligned} \mathcal{P}(\text{hit}) &= \int_{\alpha=0}^{\pi/2} \mathcal{P}(\text{hit} | B(\alpha)) \mathcal{P}(\alpha) d\alpha \\ &= \int_{\alpha=0}^{\pi/2} \frac{2A - B(\alpha)}{2\pi} \sin(\alpha) d\alpha \approx 50\%. \end{aligned} \quad (\text{C2})$$

⁴ This flat-sky approximation differs from the actual value of the solid angle by 6 per cent.